RDE Nozzle Computational Design Methodology Development and Application

Kenji Miki[1] Daniel E. Paxson[2] and H. Douglas Perkins[3]
NASA Glenn Research Center, Cleveland, Ohio 44135

Shaye Yungster[4]
HX5, Fort Walton Beach, FL 32548

The Open National Combustion Code (OpenNCC) is used to simulate the aerospike exhaust nozzle region of a rotating detonation engine (RDE). The main objectives of the current study are twofold. The first goal is to validate the proposed computational methodology using the experimental data. The second goal is to demonstrate how the validated prediction tool can be used to optimize the nozzle geometry. To achieve a significant speed-up of computational time, the computational domain in divided into two parts: a combustion region and a throat-nozzle section. In the combustion region, a validated quasi-two-dimensional in-house code is utilized to generate an unsteady RDE flow field solution just upstream of the combustor throat. Subsequently, the unsteady flow data is fed into the three-dimensional throat-nozzle section as the inflow boundary condition. This facilitates the design optimization process since the unsteady inflow can be reused, and a relatively coarse mesh (i.e., larger time-step) can be used to analyze the flow fields around the nozzle. Five nozzle designs were studied and the predicted performance (i.e., thrust) compared. The optimized nozzle was found to produce 3.2% more overall thrust than a baseline nozzle design. Without the nozzle, there is a large low-pressure region at the throat exit, which significantly reduces the overall performance. This methodology is shown to be a promising approach to explore a wide variety of nozzle geometries in a relatively short amount of time.

I. Nomenclature

AMR = Adaptive mesh refinement
CPG = Calorically perfect gas
Isp = Specific impulse [s]
MFR = Mass flow rate [kg/s]
MOT = Thrust of momentum component at the throat exit [lbf]
n = Unit vector set to be, (1,0,0)
NASA = National Aerospace and Space Administration
NPS = Naval Postgraduate School
NZT = Thrust of nozzle component [lbf]
OBT = Thrust of outer body component [lbf]
OpenNCC = Open National Combustion code

---

[1] Aerospace Engineer, AIAA member (Email: kenji.miki@nasa.gov)
[2] Aerospace Engineer, AIAA Associate Fellow.
[3] Aerospace Engineer, AIAA member
[4] Aerospace Engineer, AIAA senior member

Phi = Equivalence ratio
PRT = Thrust of pressure component at the throat exit[lbf]
P, Pt = Pressure and total pressure [Pa]
Q2D = Quasi-2D code
RDE = Rotating detonation engine
S = Surface area[m^2]
T, Tt = Temperature and total temperature [K]
u, v, w = Velocity component [m/s]
x_i, y_i = i^{th} species mass fraction and mole fractions
x, y, z = Cartesian coordinate [m]

II. Introduction

The rotating detonation engine (RDE) is currently under investigation as an approach to achieving pressure gain combustion for propulsion and power systems. The RDE typically consists of an annulus with one end open (or having a throat and/or nozzle) and the other end valved using non-mechanical, fluidic means. Fuel and oxidizer enter axially through the valved end. The detonation travels circumferentially. Combustion products exit predominantly axially through the open end. The majority of the fluid entering the device is processed by the rotating detonation wave which, as a form of confined heat release, substantially raises the pressure and temperature. The fluid is then expanded and accelerated as it travels down the annulus. Ideally, the flow exiting the device has a higher average total pressure than the flow that enters (though the averaging must be done with care due to the temporal and spatial non-uniformity of the flow). The pressure gain of an RDE can be utilized to produce thrust directly, or it can be expanded through a turbine to produce additional useful work when compared to that from conventional combustors which incur a pressure loss when operating at the same inlet conditions and fuel flow rate.

Numerous studies have been conducted to improve understanding of the effects of fuel composition, device geometry, and operating conditions on the RDE performance [1]. For instance, inside the combustor, both fuel and oxidizer enter axially through the inlet end. However, the inlet restrictions also lead to total pressure losses for the fresh charge that enters the RDE after the detonation has passed. Another important design variable for the combustor is the size of the throat, that is provided at the exhaust end [2]. Paxson performed a quasi-two-dimensional calculation [3] that showed that using an exit flow restriction (i.e., throat) can improve performance by about 10 %, compared with the basic configuration. Large performance improvements were also shown in [4] when a nozzle throat was added; however, in this semi-idealized study it was shown that instabilities can develop when the throat becomes small. Downstream of the throat, there is typically a nozzle that maximizes the thrust produced by the expanding hot combustion product. There are several design choices of an RDE combustor nozzle, such as a plug nozzle with/without a truncated cone, etc., which result in significantly different flow profiles (i.e., nozzle performance) (e.g., [5-8]). In fact, a flow field around the nozzle is very complex, composed of; compression, expansion, shear layer, shock waves, etc., which are significantly influenced by the nozzle shape and the flow properties of the exhaust. The design of a nozzle for an RDE combustor is somewhat problematic due to the spatially and temporally varying nozzle inlet flow. There is no single design pressure ratio for an RDE nozzle that can be used to determine appropriate area ratios. While there is no overall net swirl in the combustor outlet flow, there is typically a local tangential component of velocity at each circumferential location. Gas-dynamic waves are present in the flow which can propagate between the combustor and nozzle. Additionally, the boundary layer flow in the nozzle varies in both time and space, making its effect on the overall nozzle flow field difficult to predict. While an "aerospike" nozzle geometry has generally been assumed for the RDE because of the annular combustor geometry, it is not yet clear that this geometry will provide optimal performance. It is also unclear that a discrete throat is desirable for an RDE. Based on knowledge of these issues, it was determined that a relatively fast nozzle design concept exploration methodology is needed in order to explore a wide variety of nozzle geometries in a relatively short amount of time. Modeling the RDE combustor and nozzle simultaneously is not a trivial task, due to the fact that each region is controlled by different spatial and temporal

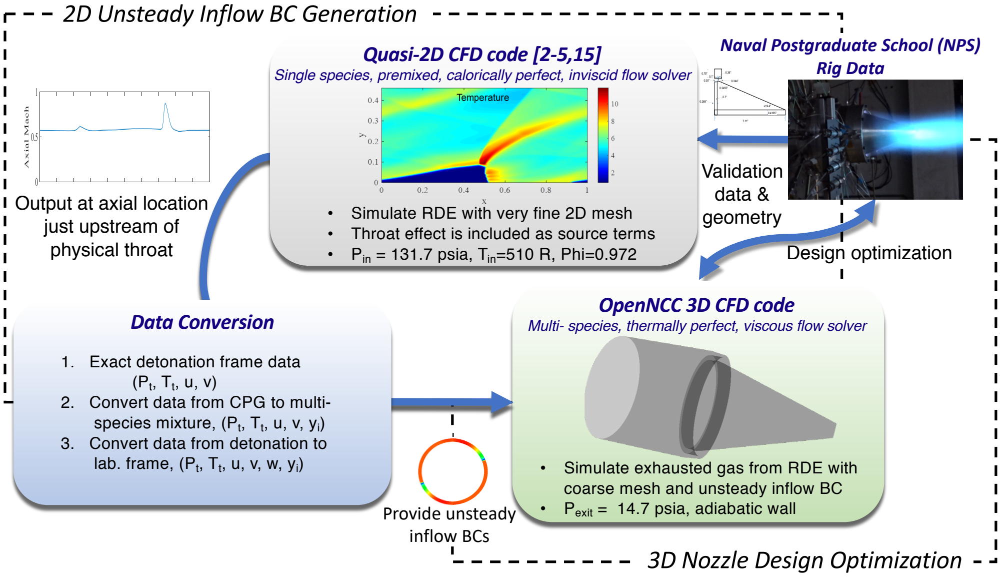

Fig. 1 Schematic of the proposed methodology of the RDE nozzle design optimization

scales. Pal et al. [9] used a commercial CFD code, CONVERGE, where an adaptive mesh refinement (AMR) technique is utilized to resolve the detonation front. With the help of AMR, they achieved a good agreement of detonation wave frequency/height with the experimental data using a relatively small mesh ~ 4.5 million) for the combustor only. Recently, Tsuboi et al. [10] performed a three-dimensional compressible Euler simulation to model an RDE engine with an unchoked aerospike nozzle (H2/Air). A relatively fine mesh (601 points in the circumferential direction) was used for the combustor, to resolve the detonation front, and much coarser mesh was used downstream. Complex unsteady flow features were well captured at different stagnation pressures (P_0 = 1.5, 2, 3, and 4 [MPa]). Although such detailed numerical simulations are desirable for an accurate prediction of the RDE performance, it is computationally expensive and not suitable for the initial nozzle design stage. Alternatively, a low-order methodology could be used to perform a parametric study of key engine design parameters [11].

In this study, using an approach similar to that of Schwer, et al [12], an approach simulating was developed for the three-dimensional unsteady calculation modeling the RDE engine with an aerospike nozzle (CH_4/Air). Here, an existing in-house quasi-2D combustor code, previously used for RDE simulations [13], was used to provide inlet boundary conditions into an 3D in-house combustor code, OpenNCC [14], which would be used to simulate the 3-D nozzle geometry (see Fig. 1). By limiting chemical kinetics calculations to the quasi-2D combustor model (modeling up to the nozzle throat), it was found that a coupled simulation limit-cycle result could be obtained within 3-5 calendar days. It was also found that an adequate solution for the combustor for some cases could be found using a simplified in-house quasi-2D code (Q2D) [5] that utilizes a simple one-step heat release model in place of a chemical kinetics calculation, further reducing overall computational time. The unsteady inlet boundary conditions are modified in the "data conversion" process in order to be used in the thermally perfect/multi-mixture 3D solver, OpenNCC, modeling from the upstream region of the throat to the exit. OpenNCC runs in a non-reacting mode [12] with a relatively coarse mesh. Although the grid resolutions of

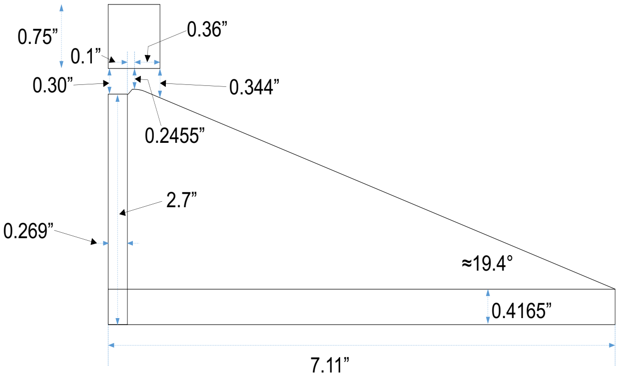

Fig. 2 Aerospike nozzle geometry used on the Naval Postgraduate School rig

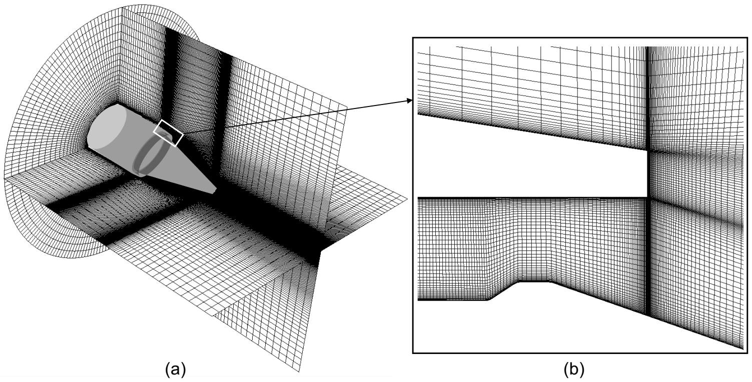

Fig. 3 Mesh of the NPS nozzle configuration, (a) overview and (b) near the edge of the outer body

Region 1 (combustor) and Region 2 (upstream region of the throat to the exit) are similar to [10], overall computational time is less expensive, since a small-time step is only used for Region 1 and a relatively large time step for Region 2. In addition, another advantageous feature of the proposed approach is that the unsteady inflow profile can be repeatedly reused as the inflow boundary condition, when simulating Region 2 with different nozzle designs. This feature significantly facilities the nozzle design optimization. It is worth mentioning that this approach is based on the assumption that the flow is chocked at the throat. As a result, the change of the nozzle shape should not significantly affect the combustor characteristics upstream.

In this paper, the proposed methodology is first validated, which is schematically shown in Fig. 1, against the experimental data acquired at the Naval Postgraduate School (NPS), using the operating condition (see Table 1) and the same “aerospike” nozzle geometry (see Fig. 2). Please note that the outer body profile (Fig. 3 (b)) is not the same as the actual profile shown in Fig. 2, but that preliminary calculations indicated that the resulting flowfield was hardly changed when using the tapered outer body of Fig. 3. The validation is performed with qualitative comparisons to the flowfield around the nozzle and quantitative comparison using the nozzle surface pressure measurement, the thrust components (gross thrust, nozzle and outer body) and the mass flow rate. A nozzle design optimization is then performed using the same unsteady inflow data used for the validation process. In this study, five different nozzle configurations are tested: the ones with different outer body sizes, the one with a short nozzle realizing a perfectly expanded flow, and the one with a curved nozzle surface with a larger initial cone angle. With help of the proposed accelerated process of calculations, it is possible to evaluate each configuration within a relatively small computational cost (~ a few days).

This paper is organized as follows. In Sec. III, the numerical approach is described including a summary of the boundary conditions (unsteady inflow BCs), the operating condition and the mesh. Results from the simulation studies are discussed in Sec. IV, and conclusions are made in Sec. V.

Table 1 Operating condition for the Quasi-2D solver for the RDE combustor

	Pt_{in} [psia]	Tt_{in} [R]	P_{exit} [psia]	phi	Air mass flow rate [kg/s]
Test condition	131.7	510	14.7	0.972	1.51

III. Computational Method and Operating Condition

To optimize an RDE nozzle configuration, two different in-house codes, Q2D and OpenNCC were selected, using for two different computational domains. For the interior region where the reaction induced by a detonation wave takes place, the quasi-two-dimensional CFD solver, Q2D [2-5,15], is used to compute the reactive, multi-wave flowfield. For the downstream region where the hot products expand along the nozzle, the three-dimensional CFD solver, OpenNCC, is used with the "unsteady" inlet boundary condition provided by Q2D. Brief explanations of these two codes are provided as follows:

Q2D uses a single species, premixed, calorically perfect gas (CPG) to investigate the RDE interior region, by solving the Euler equations in a quasi-two-dimensional manner [3]. The governing equations are integrated numerically in time, using an explicit, second-order, two-step, Runge-Kutta technique. For the inviscid flux, it utilizes the upwind scheme (Roe's approximate Riemann solver) and the MUSCL scheme for the second-order spatial accuracy. A finite rate reaction model is considered. However, the reaction is not allowed to proceed, unless the reactants are above a reaction temperature. Critical to this validation exercise, Q2D contains loss models for RDE inlets and heat transfer to the walls, both of which are substantial in the experimental rig being simulated. When the experimentally measured manifold conditions, mixture equivalence ratio, and effective inlet area were imposed on the code, it correctly predicted the mass flow rate, detonation speed, and two interior time-averaged pressures. The computed gross thrust based only on the flow at the exit throat was within 15% of the experimentally measured gross thrust. As such, it was determined that the output from this Q2D code was appropriate as input to OpenNCC. Q2D has been used for the analysis of RDE for many years at NASA Glenn Research Center (GRC) and validated with experimental data. A detailed explanation of Q2D code can be found elsewhere (e.g., [2-5,15])

OpenNCC [14] is designed for unstructured grids (i.e., any mix of three-dimensional elements: hexahedral and tetrahedral mesh) and massively parallel computing (with almost perfectly linear scalability achieved for non-spray cases up to 4000 central processing units). Regarding the numerical methods, a dual time-stepping procedure in which the solution implicitly advances in physical time and the explicit four-stage Runge–Kutta scheme is called in pseudo time, is adopted. The transport equations are spatially discretized using a cell-centered finite-volume method. The second-order Advection Upstream Splitting Method ($AUSM^+$-up) scheme [16] is used to calculate the inviscid flux minimizing the numerical dissipation with the minmod function as the limiter of the MUSCL scheme. For the turbulence model, the cubic nonlinear k-ϵ model with the wall function [17-18] and the localized-dynamic kinetic model (LDKM) [19] are available. Many previous papers and presentations (e.g., [20-24]) have shown that the combustion CFD capabilities of OpenNCC (as well as NCC) have facilitated the development/design of combustion technology at NASA GRC.

To couple these two codes at the interface that is located in the upstream region of the throat, an "unsteady" boundary condition is implemented in OpenNCC. The time-sequence of the unsteady outflow profile is collected, while running Q2D for only the combustor. The data file is composed of total pressure; total temperature; and velocity components and species concentration, at each time step. In this study, the time step and the grid spacing in circumferential direction are set to be 9.2324E-9 [s] and 0.0008 [m], respectively. The duration of data collection is long enough for a detonation wave to circumferentially travel the combustion chamber once. In OpenNCC, the unsteady outflow profile from Q2D is repeatedly used as the inflow boundary condition, under the assumption that the limit cycle was achieved during the Q2D calculation. In addition, we assume that the reactions are completed by the exit of the computational domain of the combustor, and therefore, the chemistry part in OpenNCC is turned off. Table 1 shows the operating condition using in Q2D, which resembles the experimental setup at NPS. The pressured air (Pt_{in}=131.7 [psia] and Tt_{in}=510 [R]) is specified at the inlet and, the fuel/air ratio is set to be 0.972. The resulting mass flow rate is 200.2 [lb/min]. In Q2D, a single species and treated as a calorically perfect gas (CPG) (Note that we changed from the single CPG gas of Q2D to a 3 species mixture of thermally perfect gases consisting of H2O, N2, and O2 for input into OpenNCC) is used. The unsteady exit flow fields (total pressure, total temperature, velocity components, and species concentration) are recorded and are used in the nozzle design optimization process as the inflow boundary condition in OpenNCC. Therefore, the only necessary boundary condition to be specified for the second step is the exit pressure (P_{exit} = 14.7 [psia])

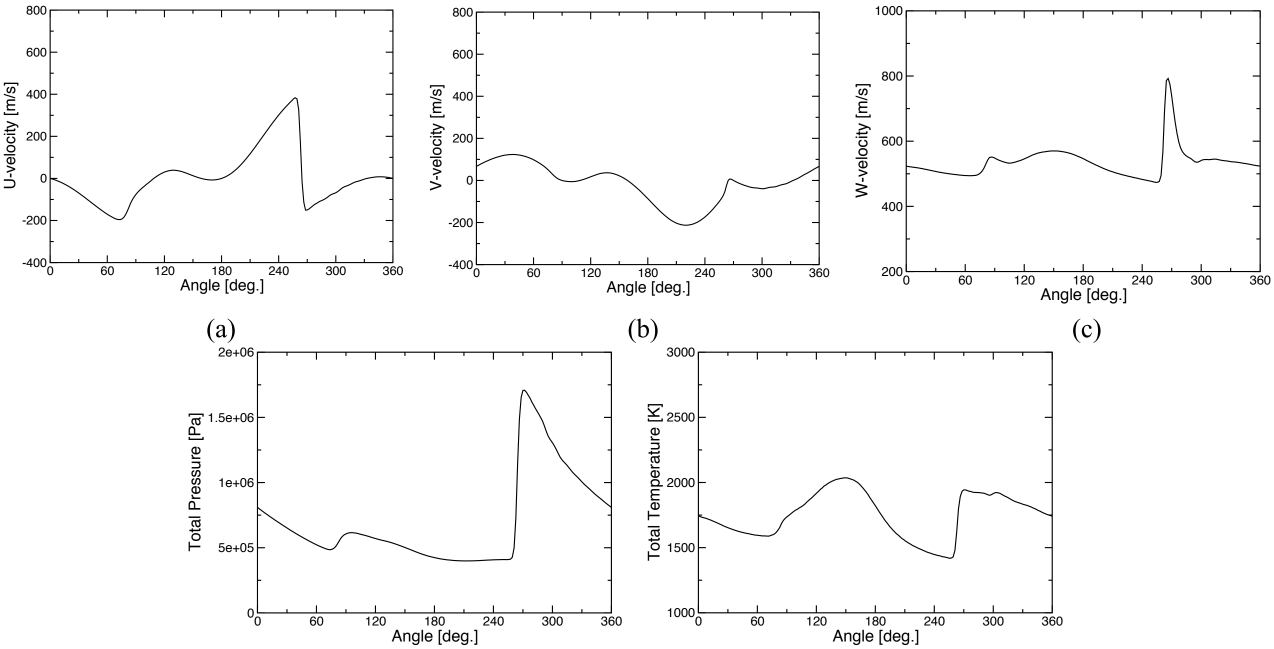

(a) (b) (c)

(d) (e)

Fig. 4 Unsteady flow fields calculated by Q2D

IV. Numerical Results

For this paper, 240 processors (Xeon E5-2680v2) of Pleiades at NASA Advanced Supercomputing facilities are routinely used. The overall computational time is approximately 3 days. The structured mesh is generated by the commercial meshing software, Pointwise, and the overall mesh count is ~600,000 elements. Figures 3 (a) and (b) show the overview of the grid and the close-up view near the edge of the outer body. Although the grid is refined in the vicinity of the solid wall, the overall mesh resolution is much coarser than one used in recent LES calculations (note that they considered only the combustor, Region 1) [25]. The quality of the mesh and the validity of the current simulation are compared with experimental data in the next subsection, and it was concluded that this mesh is adequate for capturing the basic performance of the nozzle.

Figures 4 (a)-(e) show the unsteady inflow profiles (total pressure, total temperature, u-velocity, v-velocity, and w-velocity) as a function of angle [deg.], which are calculated by the Q2D simulation (See the gray box in Fig. 1) given the operating condition (Table 1). A fine mesh adequately resolves the oblique shock at ~270 [deg.], where the pressure and velocity components drastically change.

A. Validation against the NPS Measurements

In this subsection, the nozzle flow at the operating conditions shown in Table 1 was computed and analyzed important flow field features. Figure 5 shows the instantaneous profiles of (a) the axial velocity component (u), (b) Mach number, (c) temperature and (d) static pressure. Inserted figures show s closeup view near the throat region. can

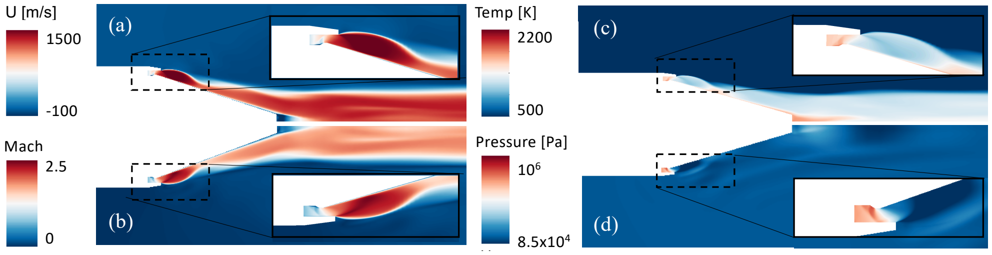

Fig. 5 Instantaneous flow fields: (a) u-velocity, (b) Mach, (c) temperature, and (d) static pressure

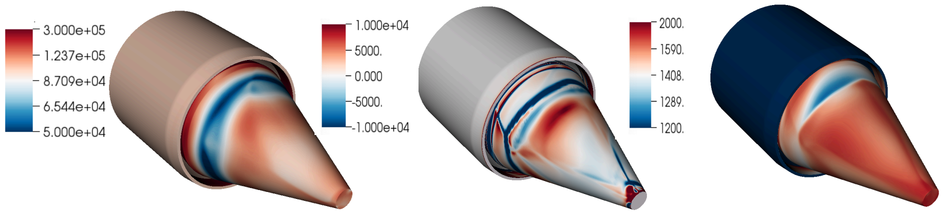

(a) Pressure (b) shear stress (c) Adiabatic wall temperature

Fig. 6 Instantaneous (a) pressure, (be) shear stress and (c) adiabatic wall temperature on the nozzle surface

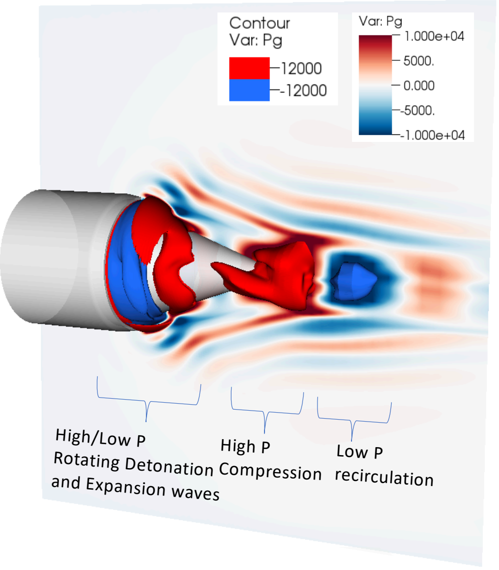

Fig. 7 Instantaneous gauge pressure profile

a small recirculation zone can be seen right before the throat, and then the flow expands/accelerates once it passes the outer body edge. The maximum Mach number is about 2.5. The flow stays close to the nozzle surface and gets compressed slightly downstream of the nozzle tip where both temperature and pressure increase. At the edge of the nozzle tip, the flow merges, forming a recirculation zone. As intended, the size of the recirculation zone is very small. Figures 6 (a)-(c) present the instantaneous pressure, shear stress, and adiabatic wall temperature at the nozzle surface. It is clearly shown that there is a low-pressure (and relatively cold temperature) region associated with the expansion wave at the throat exit. In addition, a complex distribution of the shear stress is observed. The distinguished blue region corresponds to separation of the flow due to the adverse pressure gradient. It is interesting that the steep gradient of the shear stress related to the complex inflow profiles (See Fig. 4) remains downstream of the nozzle. Figure 7 shows the instantaneous pressure fields. There is a spiral propagation generated by the two rotating detonation waves, and then high- and low-pressure regions at the tip of the nozzle. A strong dynamic motion (i.e., pressure waves) propagating toward the far-field region is observed.

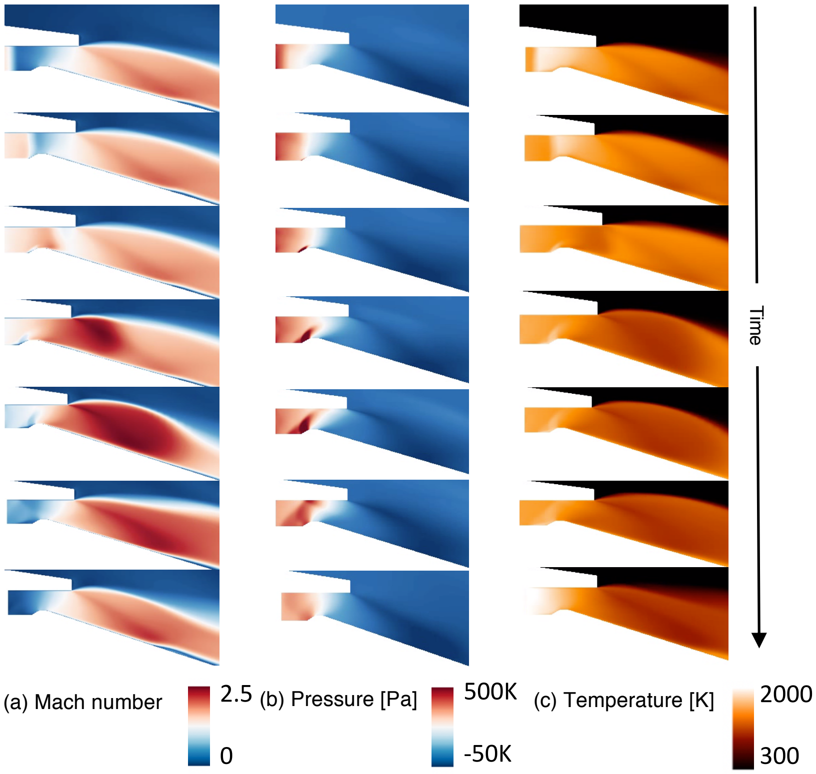

Fig. 8 Time-series of (a) Mach, (b) static pressure and (c) temperature for a half cycle.

Figure 8 shows the time-series of (a) Mach number, (b) gauge pressure and (c) temperature in the vicinity of the throat. In the first row, a high-pressure and high-Mach number flow enters into the domain. We can see the pressure increases in the region upstream of the throat, and then a strong shock wave starts forming at the left edge of the throat. The sharp edge of this throat design generates an undesirable strong shock. The flow appears to be choked at the throat and then expand after the throat. The expansion wave (i.e., low-pressure region) originates at the corner of the outer body. Due to the adverse pressure gradient by generated the expansion wave bounded by the nozzle surface, separation takes place. The size and the location of the separation bubble slightly vary over a half cycle.

Figure 9 (a) shows the time histories of the mass flow rate (MFR), and thrusts associated with components of pressure (PRT), momentum (MOT), nozzle (NZT) and outer body (OBT). The detailed locations where these components of thrust and the mass flow rate are calculated are shown in the bottom figure. The equations to evaluate these quantities are: $MFR = \int_{S_{exit}} \rho u ds$, $PRT = \int_{S_{exit}} p ds$, $MOT = \int_{S_{exit}} \rho u^2 ds$, $NZT = \int_{S_n} p\boldsymbol{n} d\boldsymbol{s}$, and OBT= $\int_{S_o} p\boldsymbol{n} d\boldsymbol{s}$, where S_{exit} is the exit area calculated at the edge of the outer body, S_n is the nozzle surface, and S_o is the entire area of the outer body. $\boldsymbol{n}$ is the unit vector pointing to the exit, $\boldsymbol{n} = (1, 0, 0)$. Each case was run to a limit cycle. The predicted mass flow rate is about 1.65 [kg/s]. There is a high-frequency oscillation super-imposed on a low-frequency oscillation. As a result, the mass flow rate oscillates by $\pm 1.5\%$. It is observed that a main contribution to the overall thrust (~ 483.7 [lbf]) comes from the momentum component (~ 441 [lbf]), and that the nozzle shows a slightly negative impact on the thrust. The outer body has a negligible thrust.

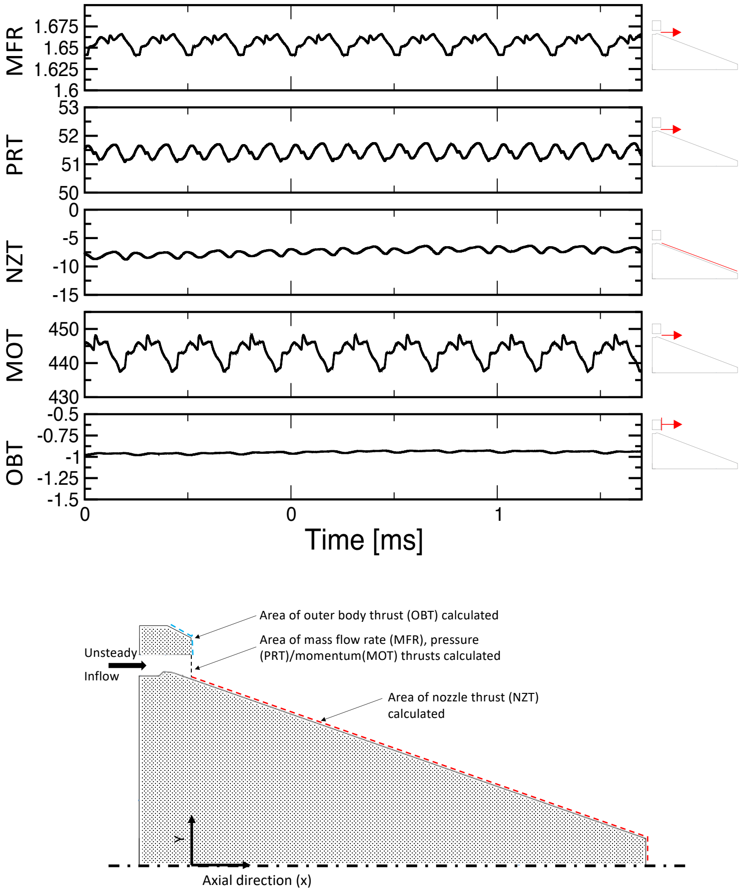

Fig. 9 (Top) Time-histories of mass flow rate, thrust associated with pressure, momentum outer body and nozzle, (bottom) schematic of thrust calculation.

In order to validate the proposed methodology, the analysis results are compared to the NPS experimental data. Figure 10 compares the instantaneous photograph from the measurement (Fig. 10 (a)) and the prediction (Fig.10 (b)). The general shape and size of the plume qualitatively appear similar for both with the exception that it is slightly rich and that some ethylene has been added to the hydrogen fuel in the experiment in order to enhance plume visibility. As mentioned above, the measured temperature contour reveals the presence of the expansion and compression waves in the middle of the nozzle. As a quantitative comparison, Table 2 summaries the mass flow rate, the gross thrust (i.e., sum of all thrusts shown in Fig.9), Isp and the thrust from the nozzle cone surface from the experiment and OpenNCC. Although the Isp's differ by about 12 % and there are some discrepancies between the two, overall agreement is satisfactory, considering the simplifications used for the computational model. It is encouraging that both the experiment and OpenNCC show that the thrust of the nozzle is negative, and that the magnitude is only a few percent of the gross thrust. Figure 11 shows the pressure profiles at the nozzle surface from the experiment (blue circle) and OpenNCC. The dashed red and blue lines indicate the throat and the edge of the outer body, respectively. Both cases show the negative region corresponding to the expansion wave at ~0.04 [m] and the local peak due to the compression wave at ~ 0.075 [m], both of which contribute significantly to the gross thrust. Although there are some discrepancies in the magnitude, the overall agreement is reasonable.

From this validation, it is concluded that the proposed methodology can successfully be used to evaluate the nozzle performance. In the next subsection, five different nozzle geometries are examined using the same unsteady inflow boundary condition.

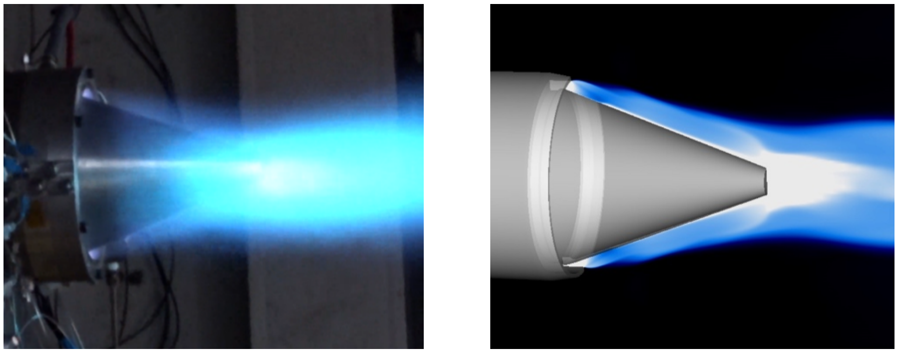

(a) Experiment (b) OpenNCC

Fig. 10 Temperature contours from (a) the experiment and (b) OpenNCC

Table 2 Summary of performance of fiver proposed nozzles and the NPS nozzle

	NPS Experiment	OpenNCC
Mass flow rate [kg/s]	1.56	1.65
Gross thrust [lbf]	413	483.7
Isp [s]	120	134
Thrust from nozzle [lbf]	-4	-7.6

B. Comparison of Five Nozzle Designs

The five different nozzle geometries shown in Figs. 12 (a)-(e) were chosen for this study. The two geometries of Case 1 (Fig. 12(a)) and Case 2 (Fig. 12(b)) are very close to the NPS nozzle, but in Case 1, the inner wall of the outer body is angled downward by 10 degrees. In Case 2, the same downward angle is used, but the outer body is extended. Case 3 (Fig. 12(c)) does not have a plug nozzle but is designed to let the flow perfectly expand on an averaged basis.

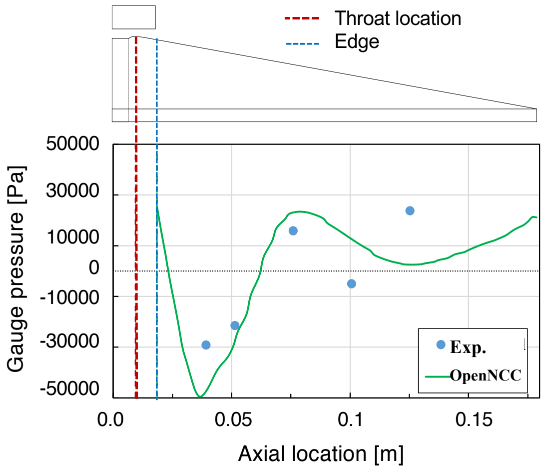

Fig. 11 Comparison of surface pressure profile between NPS experiment and OpenNCC

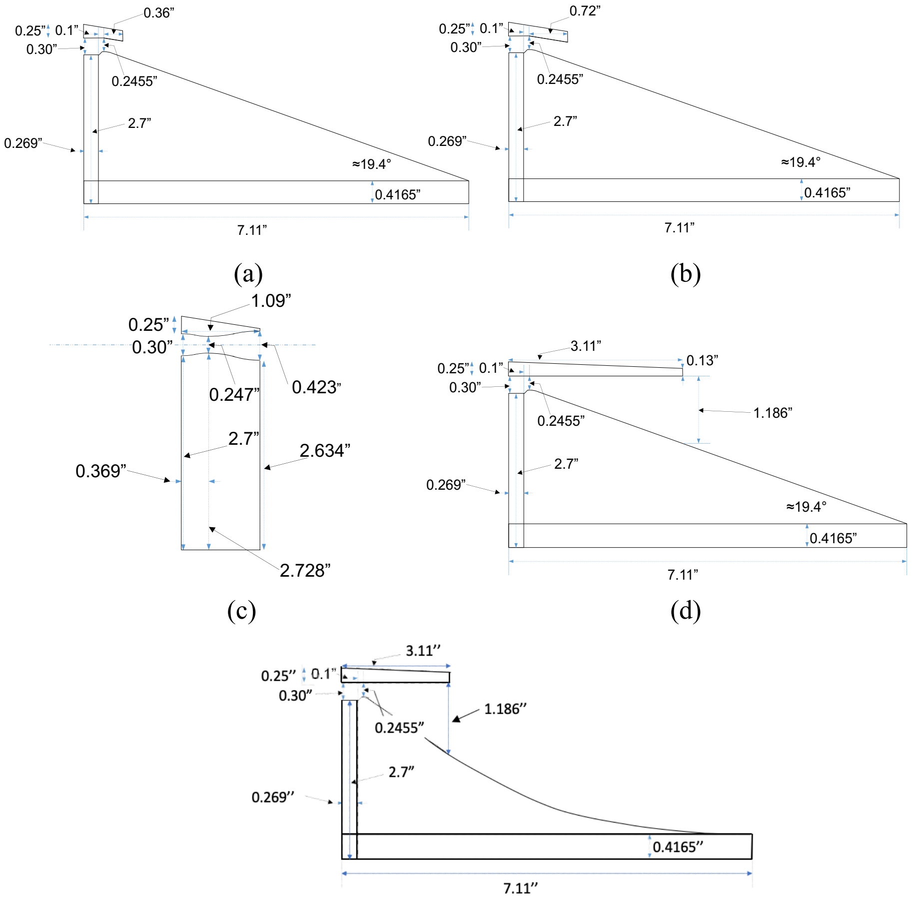

(a) (b)

(c) (d)

(e)

Fig. 12 Five geometries to be tested by OpenNCC, (a) Case 1, (b) Case 2, (c) Case 3, (d) Case 4, and (e) Case5

This geometry is particularly interesting for checking the effects of a large wake on performance. More importantly, by examining only the thrust generated by the nozzle interior, it is possible to baseline the maximum thrust that could ever be produced by this RDE exit flow. Case 4 (Fig.12 (d)) has a very large extended outer body. This nozzle was examined with high pressure variant of the imposed unsteady boundary conditions. That is to say, it was intended for an RDE with considerably higher average chamber pressure as discussed below. Finally, Case 5 (Fig.12 (e)) is similar to Case 4, but the shape of the nozzle is modified by increasing the initial cone angle from 19. 4 [deg.] to 34 [deg.].

Figure 13 (a)-(f) shows the time-averaged Mach number, temperature, pressure, and gauge pressure of the five nozzles as well as the NPS nozzle. There is a noticeable difference in Mach number profiles (first column) among the six cases although the maximum Mach number is about 2.5 for all cases. First of all, it is observed that Case 2 shows a slightly higher Mach number all along the nozzle surface, and that the exit Mach number is the highest. Also observed is a large recirculation bubble in the concave region of the nozzle surface for Case 5. Unlike the other cases, Case 4 shows distinguished flow features, showing multiple expansion and compression waves and forming a large wake. It is also found that the wake flow is very unstable, and thus the plume (green region) becomes much thicker. For the temperature and pressure profiles, all cases are similar to each other except Case 4, in which the hot product stays and rotates in the wake (low-pressure region). For Case 5, there is the elongated wake at the tip of the nozzle, where the flow expands. The last column shows the gauge pressure distributions. As expected, Case 4 shows a large negative gauge pressure region in the wake, which can be a significant drag. For Cases 1-2 and the NPS nozzle, overall profiles

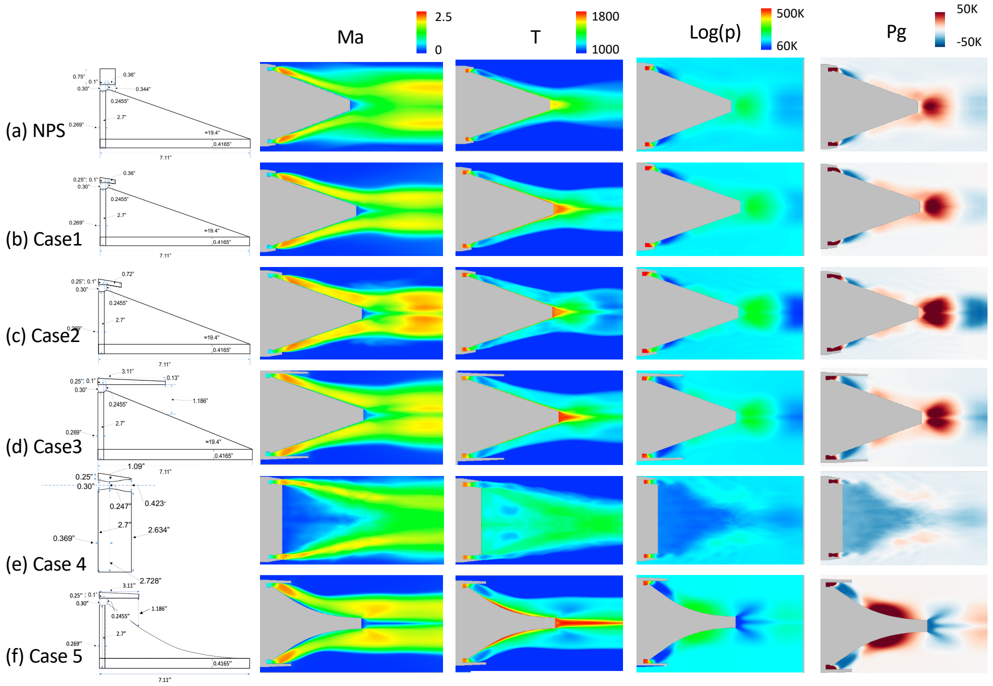

Fig. 13 Time-averaged flow fields, Mach number, temperature, pressure and gauge pressure

Table 3 Summaries of the thrust and mass flow rate from the experimental data and the prediction

Geometry	MFR [kg/s]	PRT [lbf]	NZT [lbf]	MOT [lbf]	OBT [lbf]	Total [lbf]
NPS	1.65	51.2	-7.6	441	-0.9	483.7
Case 1	1.63	91.8	-11.1	389.2	-1.7	468.2
Case 2	1.64	36.5	-5.8	460	1.2	491.9
Case 3	1.66	-16.5	17.5	500.3	-2	499.3
Case 4	1.69	-5.1	-46.5	529	0.2	478.1
Case 5	1.64	-49	35.9	487.2	-0.4	473.7

are similar in the sense that all cases show a negative pressure in the downstream region of the outer body, and then a slightly positive pressure region follows further downstream. For Case 3, since the negative pressure region ends at the edge of the outer body, the nozzle is expected to provide a positive thrust. Finally, Case 5 shows a large positive pressure region in the middle of the nozzle, generating a significant amount of thrust. However, it is important to notice that the flow expands widely after the throat, and that the negative pressure at the edge of the outer body generates a non-negligible amount of drag.

Figure 14 shows the thrust distributions at the nozzle surfaces of (a) Case 1, (b) Case 2, (c) Case 3, (e) Case 5 and (d) the NPS nozzle. The domain is divided into twenty segments and the following integration is solved for the ith segment, $NZT_i = \int_{S_{n,i}} \boldsymbol{pnds}$. The summation of these thrusts is the gross thrust of the nozzle. For the cases without a long outer body (i.e., Case 1, Case 2 and the NPS nozzle), a high-pressure region is observed upstream, following a large low-pressure region, which is problematic for this type of design. These nozzles deliver a negative net thrust. To minimize such a low-pressure region is critical while designing a nozzle. it was found to be beneficial to extend an outer body, as seen in Figs. 14 (c) and (d), to reduce the low-pressure region. Although there is a negative thrust at the nozzle tip for Case 5, this design shows the highest thrust among all cases. The summary of the performance of the five nozzle geometries as well as the NPS nozzle is present in Table 3. Although total thrusts of all cases are in the same range, the contribution from each component varies significantly. In general, as PRZ increases, MOT decreases. For Case 4, as expected, the low-pressure region in the large wake results in a significant amount of drag (~10% of total thrust).

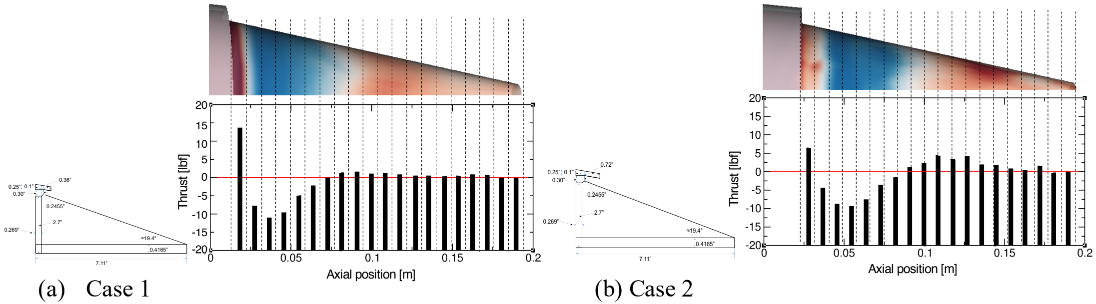

(a) Case 1 (b) Case 2

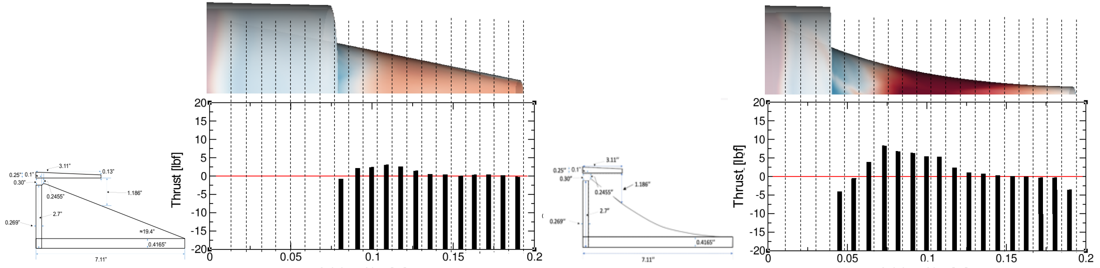

(c) Case 3 (d) Case 5

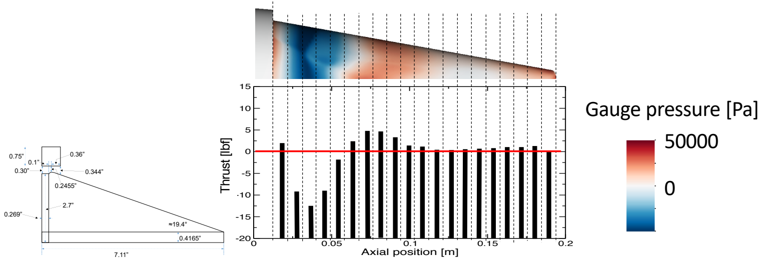

(e) NPS

Fig. 14 Distributions of thrust at 20 segments of the nozzle surfaces of (a) Case1, (b) Case 2, (c) Case 3, (d) Case 5 and (e) the NPS nozzle

For Case 5, it creates the largest thrust from the nozzle among all cases, which is compensated for PRT. Thus, the total thrust pales in comparison to the others, especially Case 2 and Case 3. From this study, Case 3 shows the best performance with a ~3.2% improvement over the NPS nozzle due to extending the outer body. Figure 15 presents the instantaneous flow fields, showing strong unsteadiness enhanced by the presence of the wake. Also, free shear layers originating from the nozzle exit are very unstable. As a result, we observe that time-variation of the thrust is large (not shown).

C. High-Pressure Operating Condition (Case 3)

In this subsection, results are presented for the Case 3 under a high-pressure condition, which is more representative of higher Mach number airbreathing, or rocket nozzle operating conditions. To this aim, the total pressure is increased by a factor of 3.9 at the unsteady inflow BC while keeping the velocity components and the total temperature the same. The time-averaged flow fields (Mach number, temperature and gauge pressure) are shown in Fig. 16, and the predicted performance of this nozzle is summarized in Table 4. It is observed that the flow fields drastically change from what are seen in Fig. 13 (d). The expansion wave (low-temperature region) is pushed downstream and covers almost the entire the nozzle surface. As a consequence, the low-pressure region is located further downstream. This results in an overall negative thrust (-26.9 [lbf]) from the nozzle. Compared the low-pressure case, although the mass flow rate increases by a factor 4.1, the gross thrust increases by a factor of 5, which is mainly attributed to the increase of MOT. In addition, it is observed that the forces from PRT and NZT are in the opposite directions in the low and high-pressure cases, however, these forces are a considerably smaller fraction of the total thrust. This suggests that this nozzle is working well, and that a simple extension of the outer body on an existing aerospike nozzle can provide reasonable performance at higher pressure ratios.

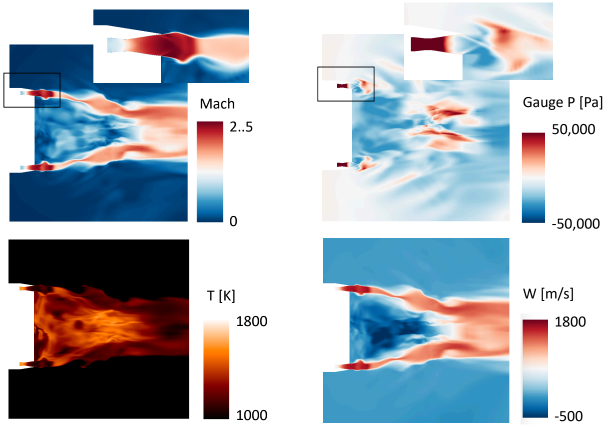

Fig. 15 Instantaneous flow field (Mach, temperature, gauge pressure and w-velocity) of Case 4

V.Conclusions

This paper has developed a computationally feasible optimization tool for an RDE nozzle by combining the quasi-two-dimensional CFD tool (Q2D) for a combustor and the three-dimensional CFD tool (OpenNCC) for the flow fields downstream of the throat of a nozzle. The novel feature of the methodology is to introduce an unsteady inflow boundary condition so that we are able to decouple the combustor and the nozzle sections. This significantly reduces overall computational time since the unsteady inflow condition is re-used for different nozzle designs under the assumption that the nozzle geometry does not significantly affect the combustion characteristics. The methodology was validated using experimental data and found that the computational predictions qualitatively and quantitatively agree with the experiment with reasonable accuracy. Then, the performance of five different nozzle designs were investigated under the same operating condition as the experiment. It was observed that extending the outer body has a positive impact on the performance by capsulating the low-pressure region inside the outer body edge. Gross thrust among these nozzles varied from 468.2 [lbf] to 499.3 [lbf]. Finally, the best nozzle was selected and tested its performance with an extended outer body under a high-power condition. Although there is a very negative thrust from the nozzle surface (<1% of the total), the expansion wave is shifted downstream and the lowest pressure region is away from the nozzle surface as intended. This proposed nozzle seems to minimize the drag effect by the expansion. This methodology is a promising tool for exploring a wide variety of nozzle geometries in a relatively short amount of time.

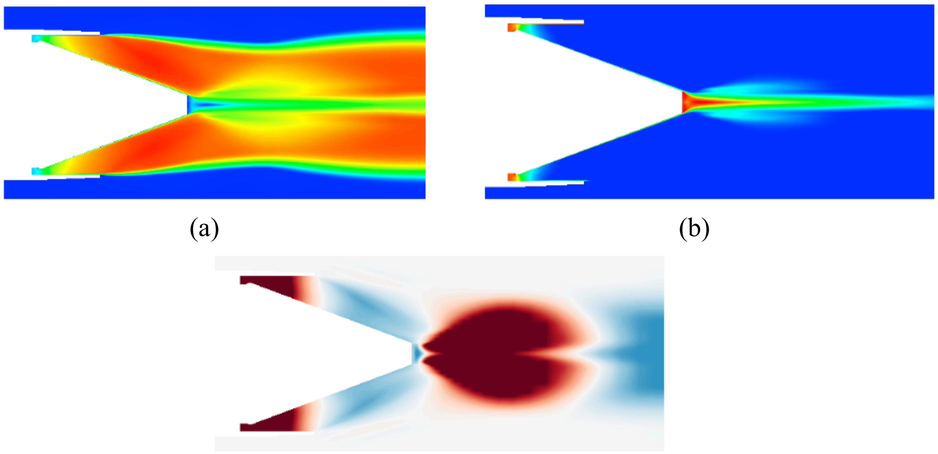

(a)

(b)

(c)

Fig. 16 Time-averaged flow fields, (a) Mach number, (b) temperature, and (c) gauge pressure of Case 3 under a high-pressure condition

Table 4 Summary of performance of Case 3 under a high-pressure condition

Condition	MFR [kg/s]	PRT [lbf]	NZT [lbf]	MOT [lbf]	OBT [lbf]	Total [lbf]
Low-Pressure	1.66	-16.5	17.5	500.3	-2	499.3
High-Pressure	6.82	54.5	-26.9	2470	-0.7	2496.9

Acknowledgments

This work was sponsored by the National Aeronautics and Space Administration Space Technology Mission Directorate's Center Innovation Fund program and Game Changing Development project. The simulations were conducted on the NASA Advanced Supercomputing (NAS) Pleiades computer cluster. Grid generation was conducted with Pointwise, and flow visualization was conducted with Visit (provided by the Lawrence Livermore National Laboratories), respectively.

References

[1] Rankin, B., Fotia, M. L., Paxson, D. E., Hoke, J. L., and Schauer, F. R., "Experimental and Numerical Evaluation of Pressure Gain Combustion in a Rotating Detonation Engine," Proceedings of the 53rd AIAA Aerospace Sciences Meeting, January 2015, AIAA Paper 2015-0877.

[2] Paxson, D., Fotia, M. L., Hoke, J., and Schauer, F., "Comparison of Numerically Simulated and Experimentally Measured Performance of a Rotating Detonation Engine," Proceedings of the 53rd AIAA Aerospace Sciences Meeting, January 2015, AIAA Paper 2015-1101.

[3] Paxson, D., "Impact of an Exhaust Throat on Semi-Idealized Rotating Detonation Engine Performance," Proceedings of the 54th AIAA Aerospace Sciences Meeting, January 2016, AIAA Paper 2016-1647.

[4] Paxson, D., Fotia, M. L., Hoke, J., and Schauer, F., "Comparison of Numerically Simulated and Experimentally Measured Performance of a Rotating Detonation Engine," Proceedings of the 53rd AIAA Aerospace Sciences Meeting, January 2015, AIAA Paper 2015-1101.

[5] Paxson, D., and Schwer, D. A., "Operational Stability Limits in Rotating Detonation Engine Numerical Simulations," Proceedings of the AIAA SciTech Forum, January 2019, AIAA Paper 2019-0748.

[6] Hagemann, G., Immich, H., and Nguyen, T. V., and Dumnov, G. E., "Advanced Rocket Nozzles," Journal of Propulsion and Power, Vol. 14, 1998, pp. 620-634.

[7] Geron, M., Paciorri, R., Nasuti, F., Filippo, S., and Martelli, E., "Transition between open and closed wake in 3D linear aerospike nozzles," Proceedings of the 41st AIAA Joint Propulsion Conference, July 2005, AIAA Paper 2005-5408.

[8] Nasuti, F., and Onofri, M., "Prediction of Open and Closed Wake in Plug Nozzles," Proceedings of the 14th Symposium on Aerothermodynamics for Space Vehicles, October 2002, ESA SP-487.

[9] Pal, P., Kumar, G., Drennan, S., and Rankin, B., "Numerical Modeling of Supersonic Combustion in a Non-Premixed Rotating Detonation Engine," Proceedings of 11th U. S. National Combustion Meeting, March 2019.

[10] Tsuboi, N., Jourdaine, N., Watanabe, T., Hayashi, A., and Kojima, T., "Three-dimensional Numerical Simulation on Hydrogen- Oxygen Rotating Detonation Engine with Unchoked Aerospike Nozzle," Proceedings of the AIAA SciTech Forum, January 2018, AIAA Paper 2018-1885.

[11] Mizener, A.-R., and Lu, F.-K., "Low-Order Parametric Analysis of a Rotating Detonation Engine in Rocket Mode," Journal of Propulsion and Power, Vol. 33, 2017, pp. 1543-1554.

[12] Schwer, D. A., Kelso, R., and Brophy, C. M., "Pressure Characteristics of an Aerospike Nozzle in a Rotating Detonation Engine", Proceedings of the 44th AIAA Joint Propulsion Conference, July 2018, AIAA Paper 2018-4968.

[13] Yungster, S., Paxson, D. E., and Perkins, H. D., "The Influence of Chemical Kinetics on Rotating Detonation Engine Numerical Simulations", Proceedings of the 66th JANNAF Propulsion Meeting, Dayton, Ohio, June 2019.

[14] Stubbs, R., and Liu, N.-S., "Preview of the National Combustion Code," Proceedings of the 33rd AIAA Joint Propulsion Conference, July 1997, AIAA Paper 1997-3114, July 1997.

[15] Paxson, D., "Numerical Analysis of a Rotating Detonation Engine in the Relative Reference Frame," Proceedings of the 52nd AIAA Aerospace Sciences Meeting, January 2014, AIAA Paper 2014-0284.

[16] Liou, M.-S., "A Sequel to AUSM, Part II: AUSM+-up for All Speeds," Journal of Computational Physics, Vol. 214, 2006, pp. 137-170.

[17] Shih, T.-H., and Lumley, J., "A New Reynolds Stress Algebraic Equation Model," Computer Methods in Applied Mechanics and Engineering, Vol. 125, 1995, pp. 287-302.

[18] Liu, N., and Shih, T.-H., "Turbulence Modeling for Very Large-Eddy Simulation," AIAA Journal, Vol. 44, 2006, pp. 687-697

[19] Kim, W.-W., and Menon, S., "A new dynamic one-equation subgrid-scale model for large eddy simulations," Proceedings of the 33rd AIAA Aerospace Sciences Meeting and Exhibit, January 1995, AIAA Paper 1995-356.

[20] Ajmani, K., and Chen, K.-H., "Unsteady-Flow Computations for the NCC," Proceedings of the 39th AIAA Aerospace Sciences Meeting and Exhibit, Reno, NV, January 2001, AIAA Paper 2001-0972.

[21] Wey, T., and Liu, N.-S., "Updates to Simulation of a Single-Element Lean-Direct Injection Combustor Using Arbitrary Polyhedral Meshes," Proceedings of the 53rd AIAA Aerospace Sciences Meeting and Exhibit, Kissimmee, FL, January 2015, pp. AIAA 2015-0099.

[22] Miki, K., Moder, J., and Liou, M.-S., “Enhancing Open National Combustion Code and Application of Energy Efficient Engine Combustor," Journal of Propulsion and Power, Vol. 34, 2018, pp. 415-427.
[23] Miki, K., Moder, J., and Liou, M.-S., “Computational study of combustor-turbine interactions," Journal of Propulsion and Power, Vol. 34, 2018, pp. 1529-1534.
[24] Miki, K., Moder, J., and Liou, M.-S., “AUSM scheme: its application to a realistic combustor configuration, the Energy Efficient Engine," Shock Waves, Vol. 29, 2019, pp. 1009-1021.
[25] Lietz, C., Desai, Y., Hargus, W., and Sankaran, V., “Parametric investigation of rotating detonation rocket engines using large eddy simulations,” Proceedings of the 55th AIAA Joint Propulsion Conference, July 2019, AIAA Paper 2019-4129.